Gomes *et al. Earth, Planets and Space* (2026) 78:157
https://doi.org/10.1186/s40623-026-02432-9

Earth, Planets and Space

FULL PAPER

Open Access

Calibration of the BepiColombo environmental radiation monitor (BERM) and cross-calibration with solar intensity X-ray and particle spectrometer (SIXS) during solar energetic particle events

António Gomes[1,2*], Marco Pinto[1,2], Carlota Cardoso[1], Rami Vanio[3], Eero Esko[4], Emilia Kilpua[4], Arto Lehtolainen[4], Philipp Oleynik[3], Beatriz Sánchez-Cano[5], Nina Dresing[3], Jan Gieseler[3], Christian Palmroos[3], Arlindo Marques[6] and Patrícia Gonçalves[1,2]

Abstract
The BepiColombo Environment Radiation Monitor (BERM) is a housekeeping instrument onboard the BepiColombo mission, capable of measuring electron, proton, and heavy-ion fluxes. Due to its quasi-continuous data acquisition throughout all mission phases, BERM provides valuable contributions to both mission operations and scientific analysis of the space radiation environment. This study presents the calibration methodology applied to the electron and proton channels of BERM, along with its validation and cross-calibration with the solar intensity and X-ray spectrometer (SIXS), also onboard of BepiColombo mission. The bow–tie method was employed to calibrate each channel by determining its effective energy and geometric factor enabling the conversion of count rates into physical fluxes. The calibration validation with SIXS data of BERM proton channels P1 to P5 result in a mean deviation in the flux lower than 6%. BERM calibrated channels proved to be consistent with SIXS measurements, enhancing the relevance of BERM to the analysis of the space radiation environment, and in particular to Solar Energetic Particles (SEP) events.

Keywords BepiColombo, BERM, Radiation monitors, Solar energetic, Heliosphere

*Correspondence:
António Gomes
antonio.pessanha.gomes@tecnico.ulisboa.pt
Full list of author information is available at the end of the article

Graphical Abstract

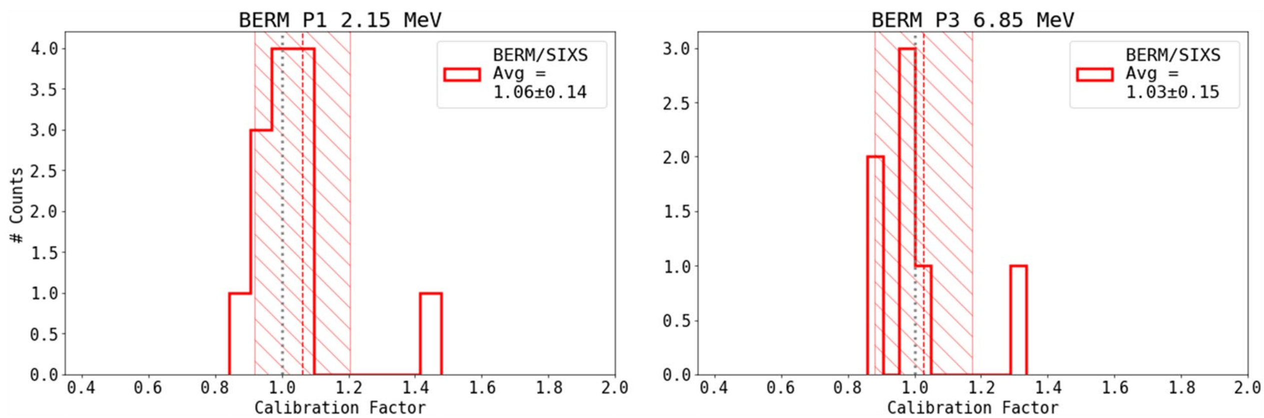

1 Introduction

BepiColombo is a joint mission of the European Space Agency (ESA) and the Japan Aerospace Exploration 32 Agency (JAXA) to explore Mercury, the closest planet to the Sun. Launched in October 2018, the mission is composed of two spacecrafts: the Mercury Planetary Orbiter (MPO) (Benkhoff et al. 2021), provided by ESA, and the Mercury Magnetospheric Orbiter (MMO) (Murakami et al. 2020), provided by JAXA. The mission will enter Mercury's orbit in late 2026, following an 8-year interplanetary cruise that includes multiple gravity-assist maneuvers of Earth, Venus, and Mercury (Benkhoff et al. 2021; Milillo et al. 2020; Sánchez-Cano et al. 2025).

The scientific objectives of BepiColombo are to investigate in detail the Mercury's surface composition, internal structure, exosphere, and magnetosphere. To achieve these goals, the MPO is equipped with several dedicated instruments: the Mercury Imaging X-ray spectrometer (MIXS), for mapping surface elemental composition via solar-induced X-ray fluorescence (Fraser et al. 2010; Bunce et al. 2020); the BepiColombo Environment Radiation Monitor (BERM), which measures high-energy charged particles throughout the mission (Pinto et al. 2022); the Solar Intensity X-ray and particle Spectrometer (SIXS), which measures solar X-ray flux and solar and magnetospheric energetic particles (Huovelin et al. 2020); the Mercury Radiometer and Thermal Infrared Spectrometer (MERTIS), for mapping surface mineralogy and temperature (Hiesinger n.d.); the BepiColombo Laser Altimeter (BELA), for measuring topography and surface morphology of Mercury (Thomas et al. 2021); the Italian Spring Accelerometer (ISA), to study Mercury's gravity field and gravity anomalies (Iafolla et al. 2010; Lucente et al. 2022); and the SERENA suite (Search for Exospheric Refilling and Emitted Natural Abundances), dedicated to characterising the neutral and ionised exosphere and surface–exosphere interactions (Orsini et al. 2010). In addition, the MPO magnetometer (MPO–MAG) characterises the Hermean magnetic field (Heyner et al. 2021).

The MMO, complements this payload with instruments designed to investigate Mercury's plasma environment. It includes the Mercury Plasma Particle Experiment (MPPE), for analysing solar wind and magnetospheric plasma (Saito et al. 2010); the MMO Magnetometer (MMO/MGF), for high-resolution magnetic field measurements (Baumjohann et al. 2010, 2020); the Plasma Wave Investigation (PWI), for electric and magnetic wave analysis (Kasaba et al. 2010, 2020); and the Mercury Dust Monitor (MDM), for detecting micrometeoroids and interplanetary dust (Nogami et al. 2010; Kobayashi et al. 2020). Together, this comprehensive payload enables simultaneous multipoint and multi-scale measurements of Mercury's environment, providing enhanced observational capabilities compared to previous missions, such as NASA's MErcury Surface, Space ENvironment, GEochemistry, 58 and Ranging (MESSENGER) (Mcnutt et al. n.d.).

Onboard the MPO, the BERM instrument plays a key role in monitoring the radiation environment throughout all mission phases. BERM continuously measures high-energy particles, including electrons (150 keV to 10 MeV), protons (1.5 to 100 MeV), and heavy ions characterized by their linear energy transfer (LET) values (Pinto et al. 2022). Despite having been designed to monitor the spacecraft health, BERM also makes scientific observations, contributing to characterizing solar energetic particless (SEPs) and galactic cosmic rays

Table 1 Electron and proton energy ranges and resolution for BERM and SIXS instruments

	BERM		SIXS	
Particle Type	**Electrons**	**Protons**	**Electrons**	**Protons**
Energy Range (MeV)	0.15–10	1.5–100	0.05–10	1–100
N° Channels	5	8	7	9

(GCRs) and supporting space weather studies. Accurate calibration of BERM's response is, therefore, essential to ensure reliable particle flux measurements, and cross-calibration with other instruments such as SIXS (Huovelin et al. 2020) that provides a valuable benchmark for validating spectral and temporal consistency across these independent detectors. This work presents the calibration methodology applied to BERM's electron and proton channels, along with its validation based on the comparison with SIXS measurements. The integration of both BERM and SIXS within the same spacecraft platform, combined with their overlapping energy ranges (see Table 1), makes SIXS an ideal instrument for cross-calibration and a valuable reference for refining BERM's calibration. A similar cross-calibration analysis was previously done with Parker Solar Probe (PSP) HET instruments resulting in a proton calibration factor of 0.74, numerical value needed to apply to HET flux to obtain BERM equivalent flux, as presented in (Khoo et al. 2024). In this work it was used one BERM proton channels with an energy range of 20.7–31.4 MeV and HET channels combined to have an energy range of 19–32 MeV.[1]

Section 2 describes the radiation environments encountered by the spacecraft during the different phases of the mission. Section 3 provides an overview of the BERM instrument, including its capabilities and operating principles. Section 4 outlines the key steps in the instrument characterisation process, which are essential for deriving accurate response functions and, consequently, reliable calibration. The bow–tie method used for channel calibration is introduced in Sect. 5, along with its specific implementation for the electron and proton channels. The main results of the calibration analysis are presented in Sect. 6, and the conclusions are summarised in Sect. 7.

2 Radiation environment

Throughout its interplanetary cruise, BepiColombo is subject to several sources of space radiation:

- *Galactic cosmic rays (GCRs)*, originating from outside the solar system, are highly energetic charged particles, primarily protons and heavy ions. Their spectrum extends from 10^6 eV to 10^{17} eV. The GCR flux is modulated by solar activity. It increases during solar minimum and decreases during solar maximum due to changes in the heliospheric magnetic field (Potgieter 2013; Honig et al. 2019). This modulation is clearly seen in BERM data throughout cruise phase, which started just before solar cycle 25 and is now at its maximum, see fig.1b).
- *Solar Energetic Particles (SEPs)*, are sporadic bursts of high-energy particles, primarily composed of protons and electrons, accelerated by solar flares and coronal mass ejections. Their intensities can vary by orders of magnitude and reach energies from tens of keV up to hundreds of MeV (Kahler 2007; Reames et al. 1997; Reames 1999; Emslie et al. 2004). BepiColombo, due to a combination of its proximity to the Sun and long cruise, which covered half of a solar cycle, has encountered numerous SEP events with relatively large intensities, see Fig. 1a). The complete list of SEP events detected by the mission until May 2024, is provided in (Sánchez-Cano et al. 2025).
- *Earth radiation belts*, encountered during BepiColombo's Earth gravity-assist, are regions of trapped high-energy electrons and protons confined by the Earth magnetic field, (Barth et al. 2003; Jun et al. 2019). Although BepiColombo was not designed to study these particles, the passage through the Van Allen belts provided an opportunity to validate the instrument's response to intense and well-known radiation environments and to perform early in-flight calibration checks. A dedicated paper on BepiColombo's Earth flyby is currently in preparation.
- *Mercury magnetosphere*, although Mercury possesses a global magnetic field, its strength is about 1% of Earth's, resulting in a very small magnetosphere (Anderson et al. 2011). Theoretical models and previous observations from missions such as MESSENGER (Mcnutt et al. n.d.) suggest that this weak magnetic field is insufficient to sustain long lived radiation belts analogous to those at Earth (Lawrence et al. 2015; Ho et al. 2011). Consequently, the occurrence of stable trapped particle populations is unlikely. Given BERM's energy ranges and the predicted electron flux levels, it is not expected that the instrument will detect trapped particles during the Mercury orbital phase, since MESSENGER has only detected electrons with energies lower than ~300 keV (Lawrence et al. 2015).
- *Solar wind particles*, a continuous outflow of charged particles, mostly protons, electrons, and alpha par-

[1] The value presented in this paper, 1.35 is the calibration factor needed to apply to BERM flux in order to obtain the HET equivalent flux, $0.74 = 1/1.35$.

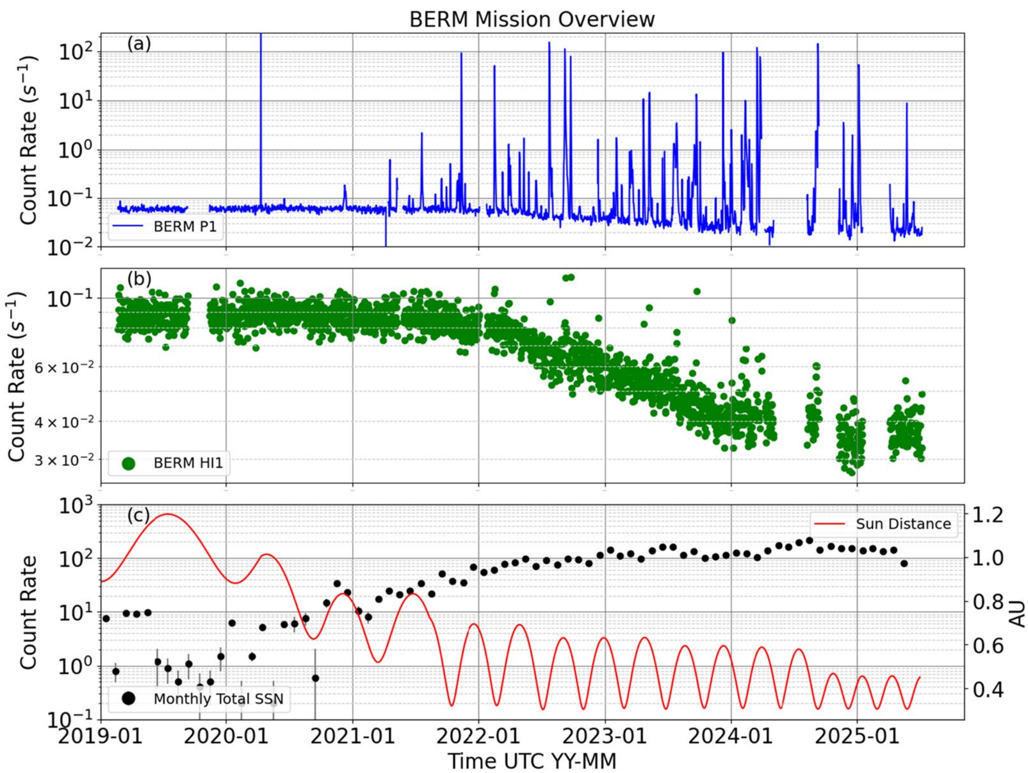

Fig. 1 Overview of BERM data throughout the cruise phase. a Overview of the first proton channel (2.15 MeV) data from BERM, highlighting the detection of SEP events during the mission (peaks above the background level). The first high peak, during April 2020, corresponds to the detection of the Earth radiation belts, during the Earth flyby. b GCR background measured by BERM's first heavy ion channel (HI1), which is sensitive to high-energy protons, approximately [1.5;3] MeV (described in more detail in Gomes (2023)). HI1 channel also detects a few SEPs, shown as data points above the background level. c Monthly total sunspot number (SSN) during the BepiColombo cruise phase (Clette n.d.), with Mission distance to the Sun plotted as a red line. This figure shows that the rate of SEP events increases with rising SSN, while the GCR flux decreases as SSN increases

ticles, from the solar corona (Yardley et al. 2024). While these particles are of lower energy than GCRs or SEPs, typically reaching energies of ~1 keV for protons, they form the background plasma environment through which BepiColombo travels (Chitta et al. 2023).

Among these particle sources, GCRs and SEPs are the dominant contributors to the high-energy particle fluxes observed by BERM.

3 Instrument description

BERM is a compact, lightweight particle detector integrated into the MPO as part of the spacecraft's housekeeping suite. Despite its operational role in BepiColombo, BERM is able to provide valuable scientific measurements of the energetic particle environment throughout the mission (see Sect. 2). The primary purpose of the instrument is to monitor the flux of high-energy particles in space providing a diagnostics tool for spacecraft anomaly investigation (Pinto et al. 2025). High-energy particles can cause short and long-term effects in spacecraft electronics, such as total ionizing dose (TID), displacement damage dose (DDD), and single event effects (SEE) (Oldham and McLean 2003; Srour et al. 2003; Dodd and Massengill 2003). TID and DDD accelerate the aging of electronic components leading to parametric failure or even malfunctions. SEEs are the result of single particle interactions within the sensitive part of the electronics. They can cause a variety of effects from single and multiple bit flips in memory cells which can disrupt operations and/or corrupt data, to latch-ups which may effectively destroy a component.

BERM employs a standard single-stack telescope, similar to those previously flown in the Standard Radiation Environment Monitor (SREM) and the MultiFunctional Spectrometer (MFS) (Mohammadzadeh et al. 2003; Arruda et al. 2016). It is composed of 11 fully depleted passivated ion-implanted planar silicon detectors, interleaved with aluminium and tantalum absorbers. This configuration allows the instrument to detect and characterize particles over a wide energy range, electrons with energies between approximately 150 keV and 10 MeV, protons between 1.5 MeV and 100 MeV, and heavy ions characterized by their LET, ranging from 1 to 50 MeV mg^{-1} cm^2 (Pinto et al. 2022). A 25 µm beryllium entrance window filters out low-energy electrons and protons, setting the lower energy limit for particle detection. The telescope's field of view is approximately 34°, oriented anti-sunward during the cruise phase. BERM processes particle events onboard, assigning them to predefined energy and species bins: five for electrons, eight for protons, and five for heavy ions (see Table 1).

3.1 Working principle

The BERM silicon detectors allow particle identification based on both the total deposited energy and the specific energy deposition pattern across the detector stack. A key parameter for this identification is the penetration depth of the particle, determined from the last detector in which energy deposition is recorded (Pinto et al. 2022). Each of the 11 silicon detectors is connected to a dedicated channel of the VA32TA2.2 ASIC, a custom application-specific integrated circuit developed by IDEAS (datasheet obtained per request from www.ideas.no.) This ASIC architecture handles signal acquisition as follows:

- Preamplifier: Converts the charge pulse from the detector into a voltage signal.
- Fast shaper and trigger: A fast shaping amplifier followed by a discriminator. In BERM's current configuration, only the fast shaper, connected to the first detector (D1), is used to generate trigger signals.
- Slow shaper: Provides shaped analog outputs optimized for energy measurement.

When a valid fast trigger is issued (i.e., the signal in D1 exceeds threshold), the ASIC outputs from all 11 detectors are sampled and digitized. The digitized signals are then sent to a field-programmable gate array (FPGA) for discriminating and further processing (Pinto et al. 2022).

The FPGA is responsible for the following operations (presented in Fig. 3):

1. Analog-to-digital conversion (ADC) and readout: The digitized signal amplitudes are read for all detectors upon a valid trigger.
2. Energy reconstruction: Energy values are reconstructed using a look-up table (LUT) that corrects the ADC output based on factors, such as detector size and noise.
3. Event validation: The FPGA discards anomalous signals, and ensures that the deposited energy profile is consistent with physical expectations of a single particle event.
4. Particle identification/binning: The type of incident particle (electron, proton, or heavy ion) is determined by analyzing the energy deposition profile. This includes identifying the detector, where maximum energy is deposited (IDMAX), and applying specific thresholds to classify the event. Once classified, events are attributed to one of the 18 predefined channels (5 for electrons, 8 for protons, 5 for heavy ions). The FPGA maintains count bins for each channel, integrating over 30-s intervals, Fig. 2.

4 Instrument characterisation

The BERM calibration is essential to ensure the physical reliability of its in-flight measurements. In a previous work (Pinto et al. 2022), the first detailed characterisation of BERM was performed, establishing response curves for each detector and determining the instrument's trigger level. This was achieved through a dedicated calibration campaign carried out with monoenergetic proton beams at the Proton Irradiation Facility (PIF) of the Paul Scherrer Institute (PSI) (Pinto et al. 2022). The objective was to determine the energy deposition response of each

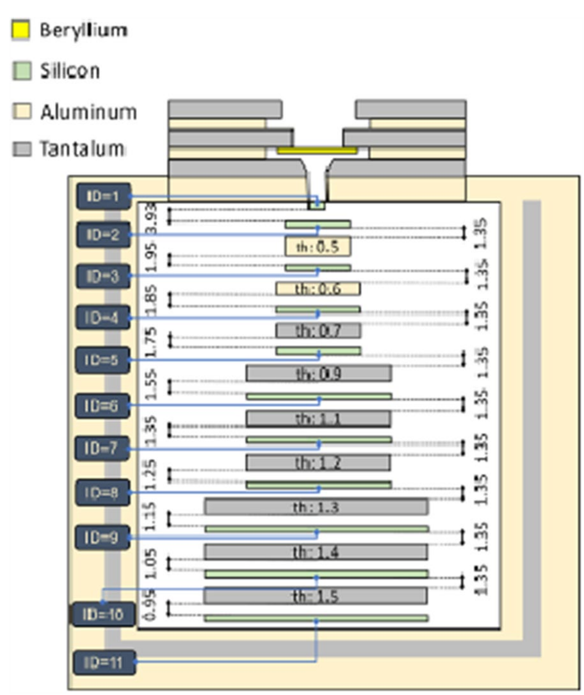

Fig. 2 Representation of BERM physical concept, with the 11 silicon detectors (green layers), tantalum collimator and shielding (grey layers), aluminium shielding (cream colour layers) and beryllium entrance (yellow layer). All units in millimetre. First detector is label as D1, second is D2 until last detectors label as D11

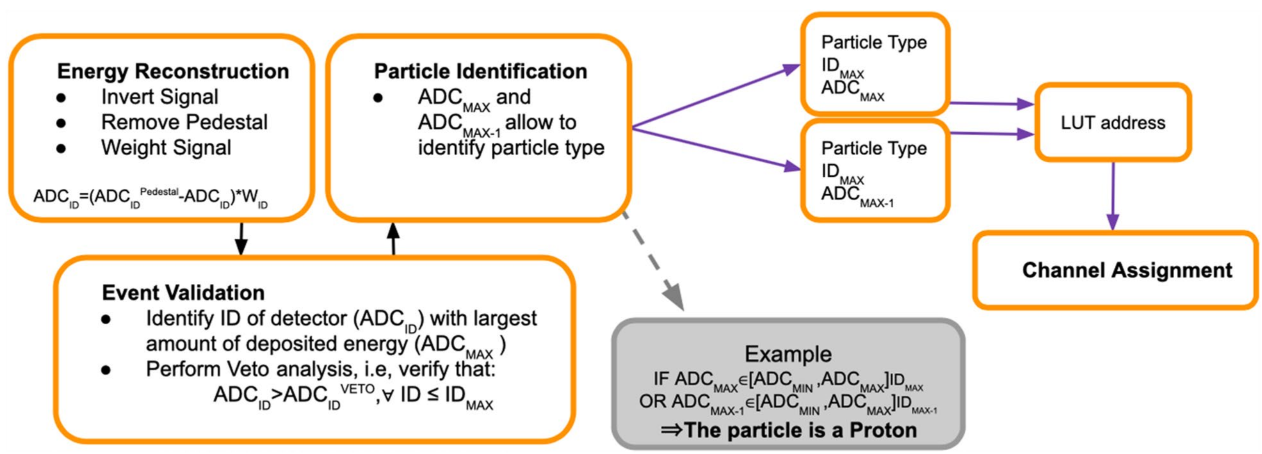

Fig. 3 Schematic representation of the BERM working principle, illustrating the sequential steps used to assign a detected particle to a specific channel. The process begins with energy reconstruction, followed by event validation and particle identification. Finally, channel assignment is performed using information stored in a look-up table (LUT). Adapted from (Cardoso 2022)

individual silicon detector under controlled laboratory conditions. Protons with energies ranging from 10 MeV to 220 MeV were directed at BERM. For each beam energy, the energy deposited in each of the 11 detectors was measured and compared with GEometry ANd Tracking (Geant4) (Agostinelli et al. 2003) simulations of the instrument. This procedure enabled direct validation of the detector stack model and the extraction of characteristic response curves for each detector.

The results of this campaign also highlighted the need for a more detailed assessment of the instrument's trigger level. Gomes (2023) carried out a detailed analysis of the trigger threshold, together with a study of electronic cross-talk between detectors and an investigation of noise correlations in adjacent detectors.

4.1 Trigger calibration

The detection of a particle in BERM is triggered when the signal in the first detector (D1) exceeds a predefined electronic threshold. Accurate knowledge of this threshold is crucial, as it determines the minimum energy a particle must deposit to be recorded. This parameter plays a particularly important role in the calibration of electron channel E1, whose sensitivity is limited to a narrow range of low deposited energies, making it highly susceptible to small variations in the threshold setting (Gomes 2023).

To calibrate the threshold in terms of deposited energy, two complementary methods were employed. The first method involved analysing the energy deposited in BERM's first detector (D1) using proton beams of varying energies. From this analysis, a linear calibration curve was obtained, where the minimum curve value corresponds to the minimum energy required to trigger the instrument (Pinto et al. 2022). The second method made use of the BERM Engineering Qualification Model (EQM) (a replica of BERM instrument) and radioactive sources of ^{137}Cs and ^{90}Sr, which emit beta particles with well-characterised energy spectra. By measuring the energy deposited in D1 under different threshold settings, the effective trigger level and its dispersion in ADC units were mapped to corresponding deposited energies (Gomes 2023). The combination of these two methods yielded a robust calibration of the D1 threshold, which was found to be 220 ± 24 keV. The relatively large uncertainty in the threshold value arises from the significant dispersion of the electronic threshold signal. Consequently, BERM is capable of detecting electrons with energies below 220 keV; however, its sensitivity in this range is considerably reduced.

4.2 Detectors cross-talk

Both Gomes (2023) and Pinto et al. (2022) reported cross-talk, the appearance of spurious signals in neighbouring detectors caused by electronic interference rather than true particle energy deposition (Gomes 2023). To analyse this effect, the same dataset of proton beam calibration was used, and a series of laboratory tests were conducted using the BERM Engineering Qualification Model (EQM) and radioactive sources. The observed energy deposition patterns consistently showed low-energy signals in neighbouring detectors that could not be attributed to actual particle interactions, confirming the presence of electronic cross-talk (Gomes 2023). This effect is particularly significant for the electron channel E1, which is sensitive to a very narrow range of deposited energy. As a result, even small changes in detector response caused by cross-talk can substantially affect the simulated response functions and the accuracy of flux reconstruction in this channel.

4.3 Noise characterisation

Electronic noise is an unavoidable feature of any analog acquisition system and must be carefully characterised to ensure reliable signal discrimination. In the case of BERM, the noise in each detector was found to follow a Gaussian distribution, with distinct mean and standard deviation values for each of the 11 layers (Pinto et al. 2022). An important finding of this study was the existence of correlated noise between adjacent detectors. That is, fluctuations in one detector's signal were statistically correlated with those in neighbouring layers. This correlation was quantified and later incorporated into the full simulation chain used to compute the response functions of BERM channels. Neglecting this effect would lead to incorrect channel assignment in some ambiguous events (Gomes 2023).

4.4 Geant4 simulations

The calibration of BERM is a crucial step to convert raw count rates into meaningful physical quantities suh as particle fluxes. This process relies on detailed Monte Carlo simulations and data analysis techniques that account for the instrument's geometry, response, and electronic processing. This chapter describes the procedures used for detector characterization, focusing on the generation of response functions via Geant4 simulations and on the application of the bow–tie method for flux reconstruction (Van Allen et al. 1974; Selesnick and Blake 2000; Boudouridis et al. 2020).

To determine the response of BERM to incident particles of various types and energies, a complete model of the instrument was implemented in the Geant4 simulation framework (Agostinelli et al. 2003). The geometry included all 11 silicon detectors, the aluminium and tantalum absorbers, the collimator structure, all shielding elements and electronic components, replicating the physical assembly as closely as possible (see Pinto et al. (2022) for more details). Detector effects such as crosstalk and threshold dispersion were also incorporated into the simulation by modifying the raw energy deposition distributions using empirical models derived from laboratory calibration data (Gomes 2023).

In these simulations, electrons and protons were generated isotropically across a wide range of initial energies. For each simulated event, the energy deposited in each of the 11 detector layers was recorded. An algorithm, replicating the signal processing logic implemented in BERM's on-board firmware, was then applied to the deposited energy of each detector. This allowed the reconstruction of the channel assignment process, effectively reproducing the instrument's binning scheme. By aggregating the results from all simulated particles, a detailed sensitivity profile was obtained for each detection channel, characterizing how it responds to different particle types and energies. These profiles constitute the instrument's response functions, as represented in Figs. 4 and 5. These response functions include corrections for the detectors' cross-talk and noise pattern and are, therefore, an update from those presented in Pinto et al. (2022).

Figure 5 shows the contamination of BERM proton and electron channels. The top panel presents the sensitivity of the electron channels to protons, together with the electron response function of the first electron channel, for comparison. The bottom panel shows the sensitivity of the proton channels to electrons, along with the proton response function of the first proton channel. As it can be seen, electron contamination in the proton channels is minimal, with the P1 response function being approximately two orders of magnitude more sensitive, and broader in energy range, than the corresponding electron response function. In contrast, proton contamination in the electron channels is non-negligible. Two types of contamination must be considered: (i) high-energy protons, which can strongly contaminate the electron channels but are absent in most SEP events analysed, as indicated by low count rates in channels P7 and P8; and (ii) low-energy protons (1.2–1.8 MeV), which contaminate only the first two electron channels over a narrow energy range. These protons are typically present with high fluxes in SEP events, potentially leading to significant contamination of electron channels E1 and E2.

4.5 SIXS instrument description

SIXS is a particle detector composed of five 150 μm-thick silicon detectors, surrounding a cubic of $5 \times 5 \times 6.3$ mm^3 CsI(Tl) scintillator, coupled to a photodiode readout (Huovelin et al. 2020). It measures electrons and protons in the energy ranges of 0.05–10 MeV and 1–100 MeV, respectively (see Table 1). SIXS covers a similar energy range to BERM; however, it provides higher energy resolution, particularly at lower energies, with 7 electron channels and 9 proton channels, compared to 5 electron and 8 proton channels for BERM.

SIXS has five viewing directions, labelled sides 0–4. Sides 1–4 are arranged in a single plane, with an angular separation of 90° between adjacent directions, while side 0 is oriented perpendicular to this plane. The BERM viewing direction is aligned approximately between SIXS sides 1 and 2, as shown in Fig. 6.

An additional distinguishing characteristic between the two instruments is their sensitivity. BERM has a nominal geometric factor of 5.5×10^{-4} cm^2 sr (Pinto et al.

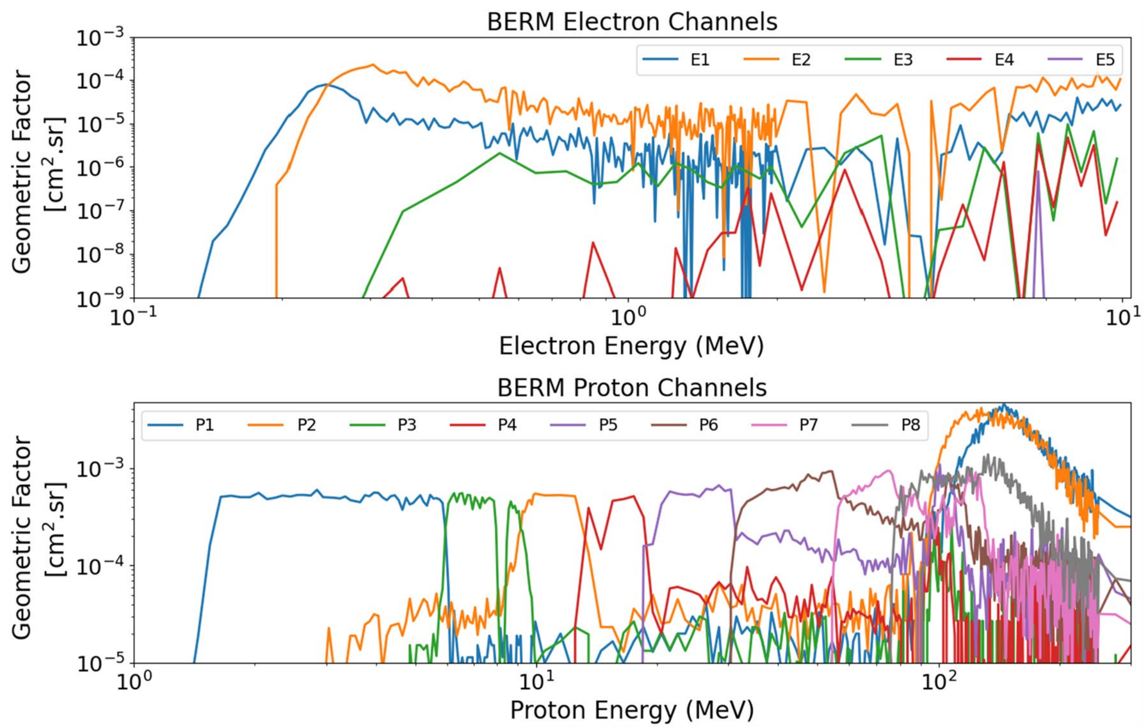

Fig. 4 Electron (top) and proton (bottom) BERM channels response functions, obtained with Geant4 (Agostinelli et al. 2003). Each line represents an instrument channel sensitivity to the different initial energies of the particles. Electron channels E1 and E2 are considered differential due to their prominent sensitivity peak around 0.25 MeV, while E3–E5 are integral channels. Proton channels exhibit a differential response function, with high-energy proton contamination for energies above ~100 MeV. This effect occurs due to protons with enough energy to penetrate the collimator

2022), whereas SIXS has a significantly larger geometric factor of 0.19 cm^2 sr (Huovelin et al. 2020). Consequently, for the same incident particle energy spectrum, BERM records substantially lower count rates, allowing to operate in conditions of higher incident flux, without saturation.

he fact that SIXS is hosted on the same spacecraft as BERM and operates over a comparable energy range, while offering higher energy resolution and count rates, makes it a highly suitable instrument for cross-calibration and validation of BERM measurements. The good agreement observed between the two instruments throughout the mission supports the robustness of their respective calibrations.

5 Flux reconstruction with bow–tie method

Once the detector response to incident particles is characterized, a method to invert the measured count rates into energy dependent fluxes is required. In this work, the bow–tie method, introduced by Van Allen et al. (1974) and further developed and used in multiple works Selesnick and Blake (2000); Boudouridis et al. (2020); Raukunen et al. (2020); Oleynik (2021),was applied. The method assumes a family of model energy spectra of the form:

$$\phi(E) = \phi_0 E^{-\gamma} \tag{1}$$

where $\phi(E)$ is the differential particle flux, γ is the spectral index (spanning from 0.5 to 6.5 in this analysis), and ϕ_0 is a normalization factor. While other spectral shapes can be used, the power-law was selected, because it provides a sufficiently accurate approximation of the local energy spectrum within the energy range, where each BERM channel is most sensitive. Although fitting the full particle spectrum of SEPs, across several orders of magnitude in energy would require more complex spectral shapes, this is not necessary for calibration purposes. The power-law function offers a simple and robust solution that satisfies this requirement. We also tested the method using other more complex functions as the broken power law, used in Dresing et al. (2020); Strauss et al. (2020); Rodríguez-García et al. (2025), but yielding no improvement in calibration accuracy. For each value of γ, the model spectrum is convolved with the detector's response function $RF(E)$, yielding an expected count rate for each channel:

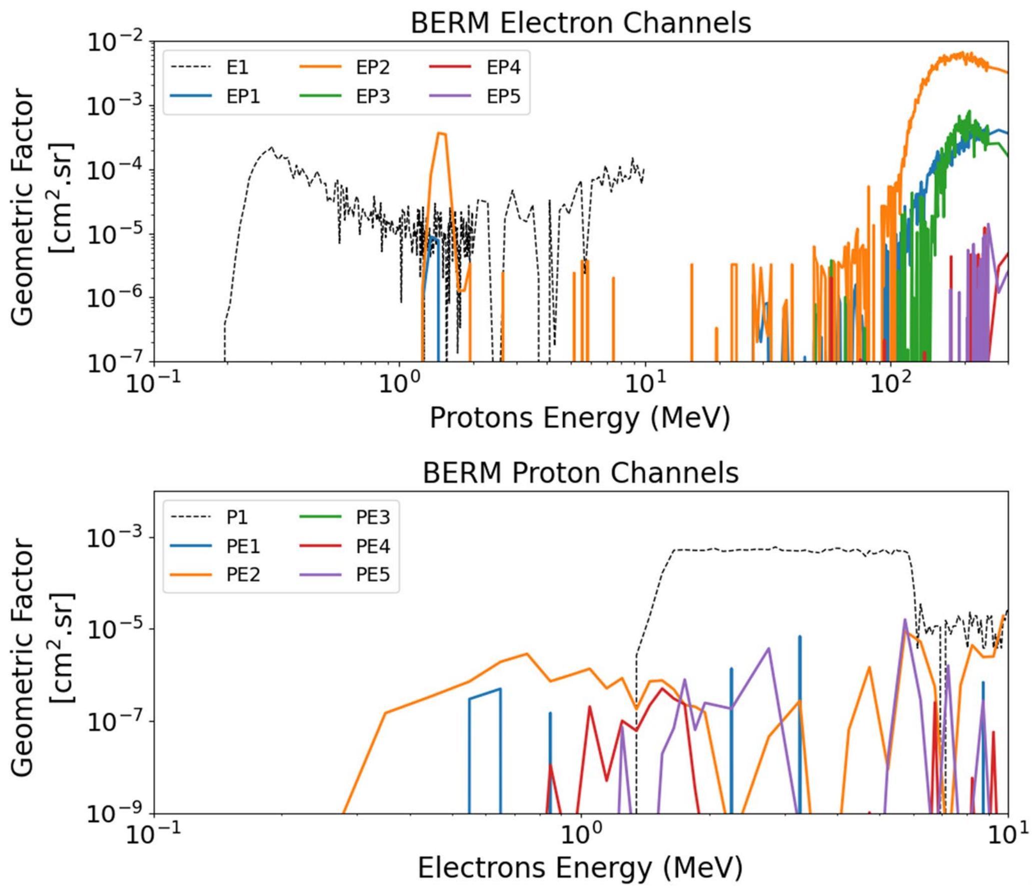

Fig. 5 Contamination response functions. Electron channels' sensitivity to protons (top) and proton channels' sensitivity to electrons (bottom), obtained with Geant4 (Agostinelli et al. 2003). For comparison, a response function of the intended particle type for that channel was added as black dashed line in both plots. Electron contamination in proton channels is almost negligible due to the difference in intensity and energy range, while proton contamination in electron channels has to be taken in consideration whenever the radiation environment includes high proton fluxes

$$C = \int_0^\infty RF(E) \cdot \phi(E)\, dE \tag{2}$$

At this point the channel in consideration needs to be characterized as integral or differential. Integral channels are sensitive to particles above a certain energy (e.g., channel E3, see Fig. 4), while differential channels are sensitive to particles within an energy interval (e.g., channel P1, see Fig. 4). Electron channel E3 The bow–tie curves are defined based on the expected count rate value as following (differential equation 3, integral equation 4):

$$GdE(E) = \frac{\int_0^\infty RF(E') \cdot \phi(E')\, dE'}{\phi(E)} \tag{3}$$

$$G_I(E) = \frac{\int_0^\infty RF(E') \cdot \phi(E')\, dE'}{\int_E^\infty \phi(E'')\, dE''} \tag{4}$$

For computational efficiency, the integration boundaries in Eqs. 3 and 4 were adjusted to avoid 0 and ∞. In the numerators, the lower boundary at 0 was replaced with a value below the onset of the response function (0.1 MeV for electrons and 1 MeV for protons), while the upper boundary ∞ was replaced with the maximum energy considered in the response function simulations. These modifications do not affect the results, since whenever $RF(E) = 0$, the corresponding contribution to the integral is also zero. For the denominator in Eq. 4, the upper limit ∞ was replaced with a value several orders of magnitude higher than the maximum energy used in the analysis, in order to prevent computational issues.

These curves are computed for a range of γ values that are consistence with the radiation environment encounter by the instrument, generating a set of bow–tie curves. The point of minimal variance in the distribution of the set of curves defines the effective energy E_{eff} and the corresponding geometric factor G_{eff} of the channel.

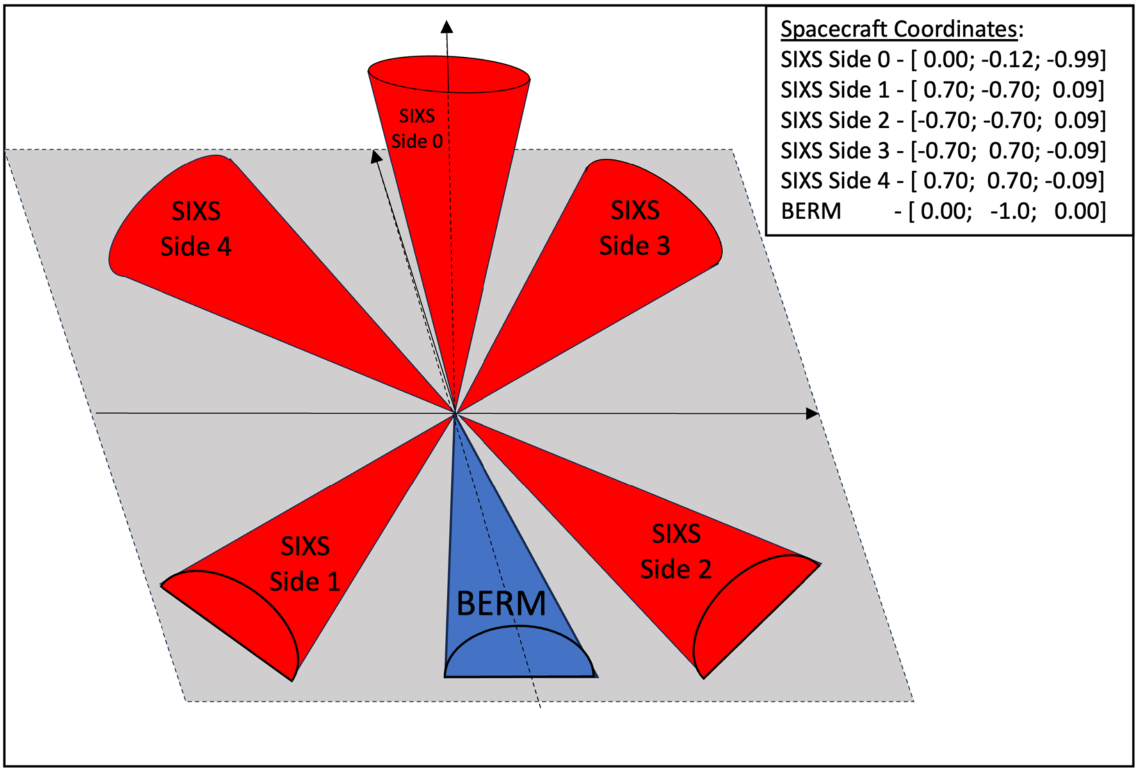

Fig. 6 Relation between SIXS and BERM viewing directions. SIXS sides 1–4 lie in the same plane with an angular separation of 90°, while side 0 is oriented perpendicular to this plane. BERM viewing direction is in the same plane as SIXS sides 1–4. The field of view is not shown to scale

Using the measured count rate C_{rate} for each bin and the integration time Δt, the particle flux at E_{eff} is then estimated as

$$\phi(E_{\text{eff}}) = \frac{C_{\text{rate}}}{G_{\text{eff}}.\Delta t}.$$

5.1 Electron channel flux reconstructions

Figure 7 shows the results of the bow–tie method applied to the calibration of BERM electron channels E1, E2, and E3. Although these channels do not exhibit a clearly defined energy range with consistently high sensitivity, channels E1 and E2 were classified as differential channels due to their prominent sensitivity peak around 0.25 MeV. In contrast, channel E3 was treated as an integral channel, as it lacks any specific energy range with a significantly higher geometric factor. Channels E4 and E5 were not calibrated using the bow–tie method due to their low overall sensitivity, that translates into a very low count rate in flight. The low sensitivity in all electron channels, but in particular in channels E4 and E5, can be explained by the high trigger level of the instrument. To trigger an event, the particle must deposit a minimum of 220 ± 24 keV in the first detector (Pinto et al. 2022), which highly limits the sensitivity of the instrument to electrons.

5.2 Proton channel flux reconstructions

As mentioned above in this section, the bow–tie method relies on a family of model spectra, which may be defined by one or more free parameters. In this work, a power-law function was used, characterized by a single parameter, the spectral index. The range of parameter values chosen for the method should reflect the spectral conditions expected to be encountered by the instrument during operation. For BERM proton channels, it was found that the choice of spectral index range can significantly influence the results, as illustrated in Fig. 8 (see list of spectral index ranges in Table 2). This figure shows the variation in the calculated effective energy and geometric factor as a function of selected spectral index ranges to test the bow–tie method. These results highlight the strong sensitivity of the bow–tie calibration when applied to the BERM proton response function. Small changes in the chosen spectral index range can lead to completely different calibration outcomes. This effect is especially pronounced for ranges centred at lower spectral indices, where both the effective energy and the geometric factor decrease by nearly an order of magnitude when moving

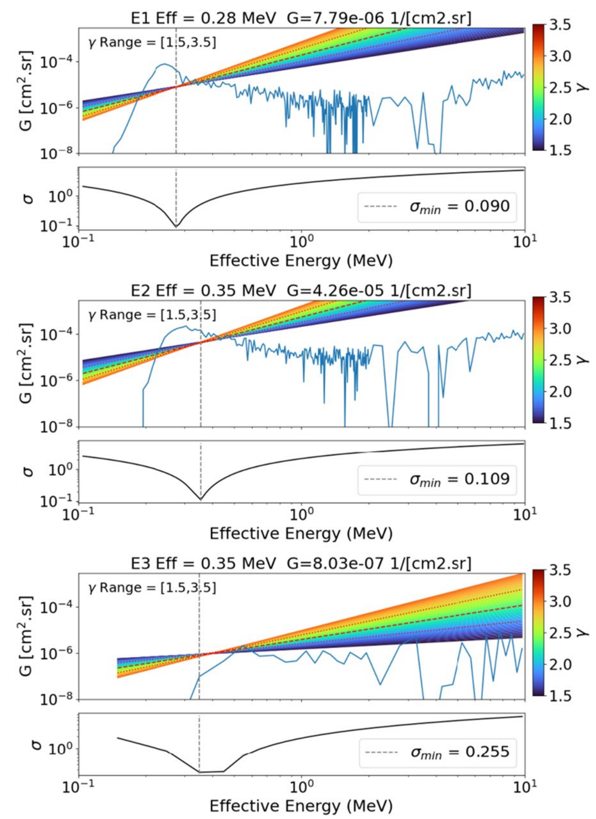

Fig. 7 Bow–tie method applied to BERM electron channels E1, E2, and E3. The blue line represents the response function of each channel. The colored lines, ranging from blue to red, correspond to the bow–tie curves computed for different spectral indices γ within the range [1.5, 3.5], applied to a power law function (Eq. 1). The black curve indicates the energy-dependent dispersion of the bow–tie curves. The red dashed line, along with the red dotted lines, represent the 50%, 25%, and 75% percentiles of the bow–tie curves. BERM electron channels E4 and E5 were not calibrated with the bow–tie method due to the low sensitivity

from a spectral index range of [0.5; 1.5] to [1.5; 2.5]. Figure 8 also shows that the central value of the spectral index range has a greater influence on the calibration parameters than the width of the range.

5.3 Proton channels—bow–tie parameter selection

To study the dependence of the bow–tie method with the spectral index, we applied it across a selection of spectral index ranges, from 0.5 to 6.5, with different widths, as summarized in Table 2. This method yields to obtain calibration factors that are applied to all proton BERM data, regardless of the spectral index. By comparing BERM flux data (obtained under different assumptions in the bow–tie method) for multiple solar events, we identified the calibration parameters that provide the best performance under the conditions typically encountered by BERM. The quality of the results is assessed through the dispersion observed in the comparison between BERM and SIXS data. Since SIXS data uses a single, consistent calibration across the entire dataset analyzed in this work, the comparison with BERM data (calibrated using the final parameters derived in this analysis) allows us to characterize the quality of the final BERM calibration across different spectral indices. The method is summarized in the flowchart of Fig. 9 and it consists of three steps:

- *Bow–tie*—Compute the bow–tie using a power-law function (Eq. 1) for the 13 γ ranges mention in Table 2. The output of this step is a set of 13 possible BERM calibration, which one of those will be use as the final calibration for BERM proton channels.
- *Comparison*—As described in Sect. 5.2 and Fig. 8, the γ ranges used in the bow–tie heavily impacts the method output. For that reason the chosen of the γ range used, was made based on the comparison of BERM calibrated data (for each different calibration) and SIXS data. This analysis was performed using data from 13 6-h time windows, selected from various SEP events detected by both instruments. From this comparison, for each channel a calibration factor (CF) was computed using Eq. 5, for each γ range and time period, resulting in 11x13=143 CF values. After this point, it was computed a mean CF for each γ range (for each channel), as shown if Fig.11, with channels ID in the x axis and $|CF-1|$ on the y axis. The choice of using $|CF-1|$ facilitates the visual identification of the minimum value of CF.
- *Selection*—From the 13 possible calibrations it was selected, for each channel, the one with the CF value closest to 1. The result of this step is one pair of calibration parameters GF;E_{eff} per channel. For P1,P2 and P3 was used the range [3,5;4,5], for channel P4 the range [1,5;3,5], and for channels P5,P6,P7 and P8 the range [0,5;2,5].

$$CF_{ch} = \frac{\text{BERM Flux}_{ch}}{\text{SIXS Flux}(E_{ch})} \tag{5}$$

Here CF_{ch} is the channel calibration factor, BERM Flux_{ch} is the flux of the same channel and SIXS $\text{Flux}(E_{ch})$ is the flux obtained with the SIXS spectrum fit for the energy of the same BERM channel. The CF value is defined as the factor applied to SIXS data to obtain the corresponding BERM data (or, equivalently, by which BERM data are divided to obtain the corresponding SIXS data). The CF also quantifies the differences between BERM and SIXS measurements: $CF=1$ indicates that both instruments

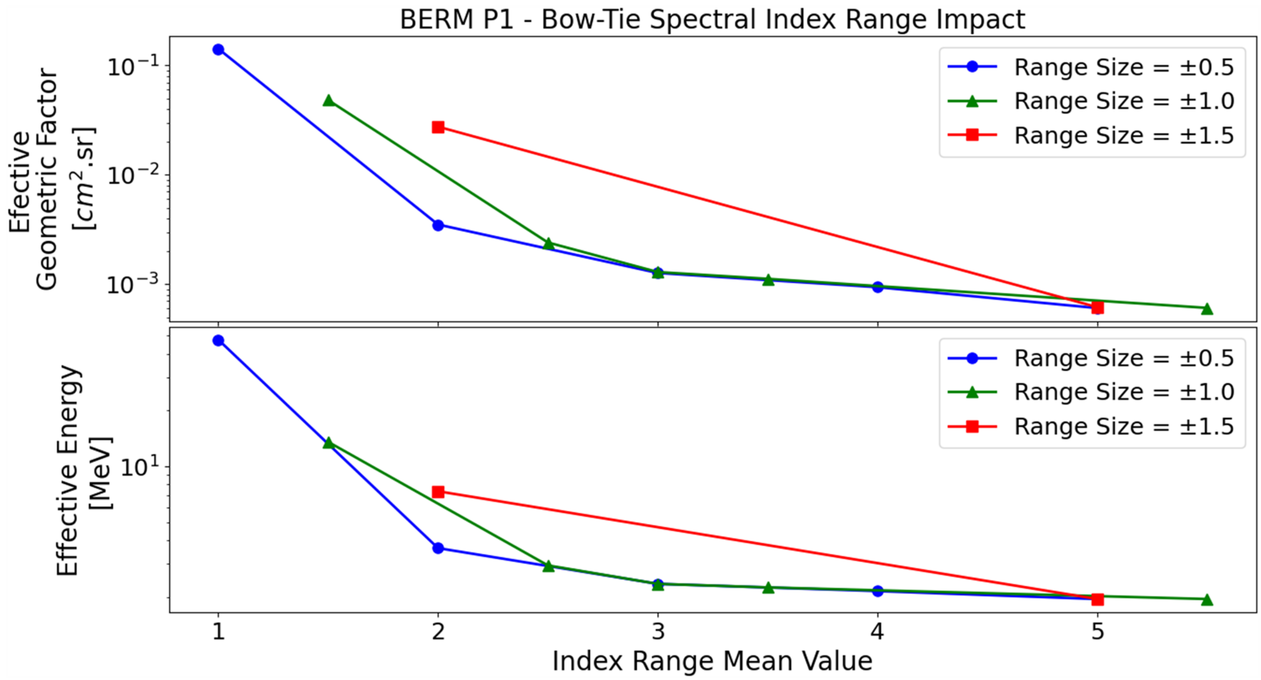

Fig. 8 Impact on the bow–tie result of the first proton channel (P1) for different spectral index ranges, listed in Table 2. The top panel shows the effective geometric factor variation with spectral index range, and the bottom shows the variation of the effective energy. Each data point is positioned at the midpoint of its corresponding spectral index range. To obtain these parameters, the bow–tie method was employed assuming a power-law spectrum (Eq. 1)

Table 2 Spectral index ranges used to apply the bow–tie method assuming a power law function (Eq. 1). Each line correspond to ranges with the same width

Width	Spectral Index Ranges γ [min;max]				
1	[0.5;1.5]	[1.5;2.5]	[2.5;3.5]	[3.5;4.5]	[4.5;5.5]
2	[0.5;2.5]	[1.5;3.5]	[2.0;4.0]	[2.5;4.5]	[4.5;6.5]
3	[0.5;3.5]	[3.5;6.5]			
5	[0.5;5.5]				

are measuring (in average) the same particle flux, whereas $CF > 1$ ($CF < 1$) indicates that BERM measures a higher (lower) particle flux than SIXS.

The selected intervals, highlighted by red shaded areas in Fig. 10 correspond to periods during decay phases of SEP events when both instruments observed proton fluxes under near-isotropic conditions. We sample as many time windows as possible, so that the evaluation was performed across a broad range of spectral shapes. All events from time periods when SIXS and BERM were operated at the same time (Sánchez-Cano et al. 2025) (unlike BERM, SIXS is not continuously switched on) and simultaneously measured SEP events also detected by BERM, with sufficient counts to make a statistical significant analysis, were selected. For this analysis, omnidirectional fluxes from SIXS were used, mean values of the measurements of all available sides of the instrument (sides 0, 1 and 2),[2] this method increases the statistics of the data without compromising the analysis, since all time periods used were under near-isotropic conditions.

For the analysis of each time window within the SEP events, the cumulative SIXS energy spectrum, for each selected periods (see Fig. 10), was fitted with a Band function, defined as (see Band et al. (1993); Yu et al. (2022)):

$$\text{Flux}_{\text{ch}} = \begin{cases} A \cdot E^{-\gamma_a} \cdot \exp\left(-\dfrac{E}{E_0}\right), & \text{if } E \leq (\Delta\gamma) \cdot E_0, \\ A \cdot E^{-\gamma_b} \cdot [(\Delta\gamma) \cdot E_0]^{\Delta\gamma} \cdot \exp(-\Delta\gamma), & \text{if } E \geq (\Delta\gamma) \cdot E_0. \end{cases} \quad (6)$$

The parameters γ_a and γ_b are the spectral indices that describe the low-energy and high-energy regimes of the spectrum, respectively. The difference between them is defined as $\Delta\gamma = \gamma_b - \gamma_a$. The parameter E_0 represents the characteristic energy at which the transition between

[2] Sides 3 and 4 of SIXS were not used in the analysis due to occasional noise problems in side 3 (Oleynik et al. n.d.), and total obstruction of side 4, by the spacecraft cruise shield, during the cruise phase of the mission (Sánchez-Cano et al. 2025).

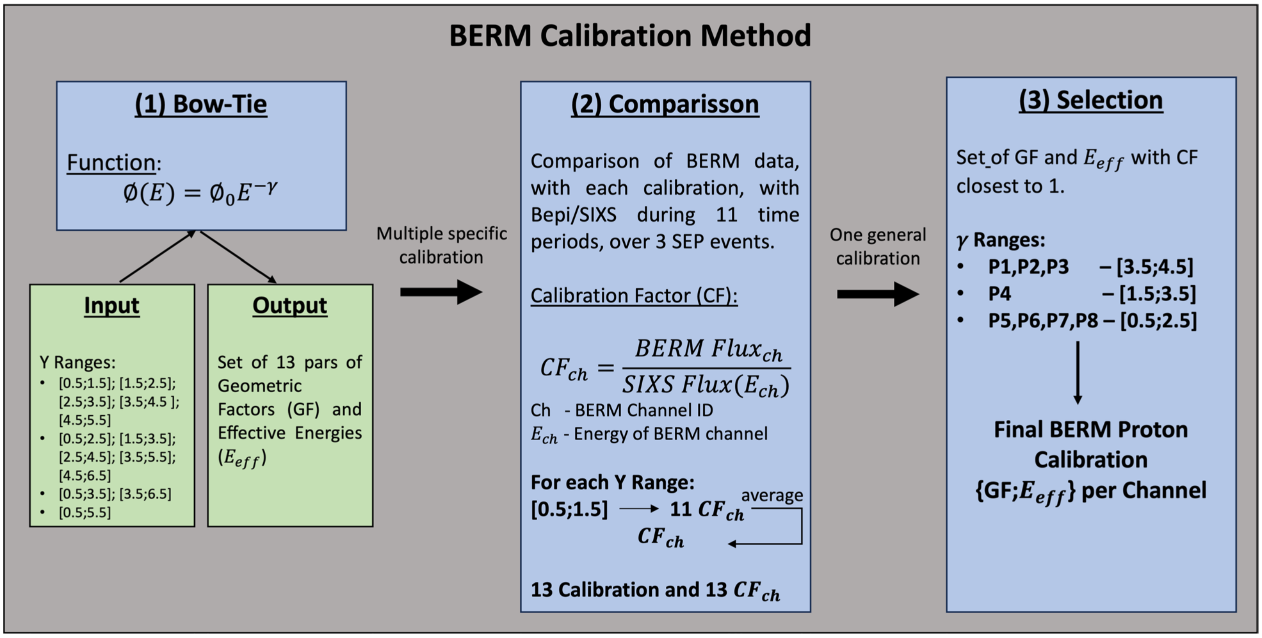

Fig. 9 Flowchart summarizing the calibration procedure for the BERM proton channels. The process is divided into three main steps: (1) computation of bow–tie functions for multiple γ ranges; (2) comparison of the resulting calibrations with SIXS measurements; and (3) selection of the optimal calibration parameters to be applied to the BERM proton data

the two spectral components occurs, and A is the normalization constant (or amplitude) of the spectrum.

The corresponding BERM data were then compared with the SIXS flux at the effective energies of the BERM channels, as shown in Figs. 13, 14 and 15, for all selected time intervals. These figures present the BERM and SIXS energy spectrum, with background subtracted and the ban function fit applied to SIXS data. In the figures is presented the fit parameters, along with the CF obtained for each BERM channel available. All selected time intervals contributed to the analysis with different spectra characteristics, with fitted Band function parameters spanning the ranges $\gamma_a = [1.20, 2.87]$, $\gamma_b = [2.72, 4.79]$, and $E_0 = [3.84, 16.44]$. The complete set of spectrums computed for SIXS and BERM, the parameters obtained and the CF values for each BERM proton channel are presented in App. A, in Figs. 13, 14 and 15.

5.4 Results and validation

Table 3 presents the calibration parameters obtained for BERM electron and proton channels using the methods described above. As shown by the bow–tie results, proton channels whose response functions exhibit smaller differences between the regions of low and high sensitivity (see Fig. 4) can yield effective energies located outside their nominal high-sensitivity energy ranges. This occurs, because, in such cases, the contributions from lower sensitivity regions are no longer negligible. This effect is evident in channel P2, which has an effective energy of $E_{\text{eff}} = 4.85$ MeV despite its maximum sensitivity corresponding to protons between 9 and 13 MeV, and in channel P5, with $E_{\text{eff}} = 41.5$ MeV, which has maximum sensitivity for protons with energies between 19 and 31 MeV. This mismatch also results in larger uncertainties in the estimated geometric factor of these channels.

The results also reveal the impact of contamination by high-energy protons ($E > 100$ MeV). These particles can penetrate the instrument's collimator and produce a secondary peak in the proton and electron channel response functions. This contamination affects the channels in two distinct ways. In channels P1 and P2, the secondary sensitivity peak is significantly higher and located much farther in energy from the primary sensitivity peak. This is a consequence of particles entering entering through the nominal aperture, which can impact the data from these channels if the proton flux above 100 MeV is high (as indicated by increased count rates in channel P8). In contrast, for channels P6 and P7, the secondary sensitivity peak is lower in amplitude but much closer in energy to the primary peak. This results in a wider energy band of high sensitivity with a gap between the two peaks, which increases the uncertainty in the geometric factor estimation for these channels.

As discussed in Sect. 5.1, electron channels E1 and E2 do not exhibit a clearly defined energy range with

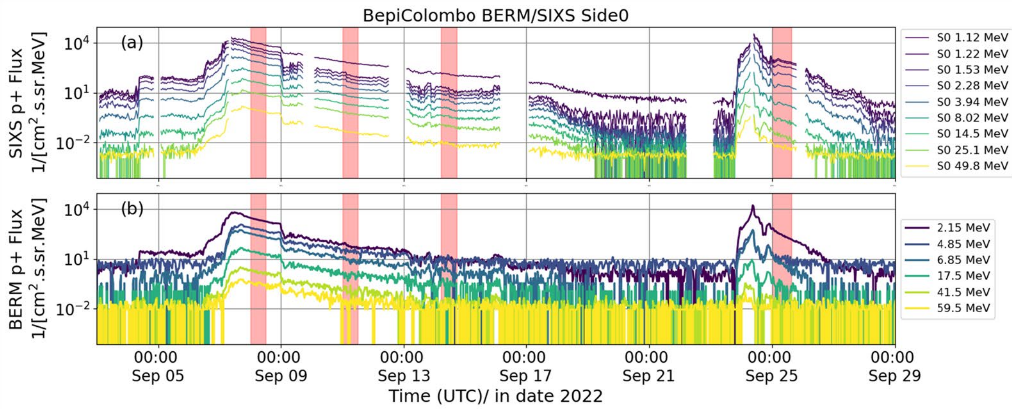

(a) 2022 September 03

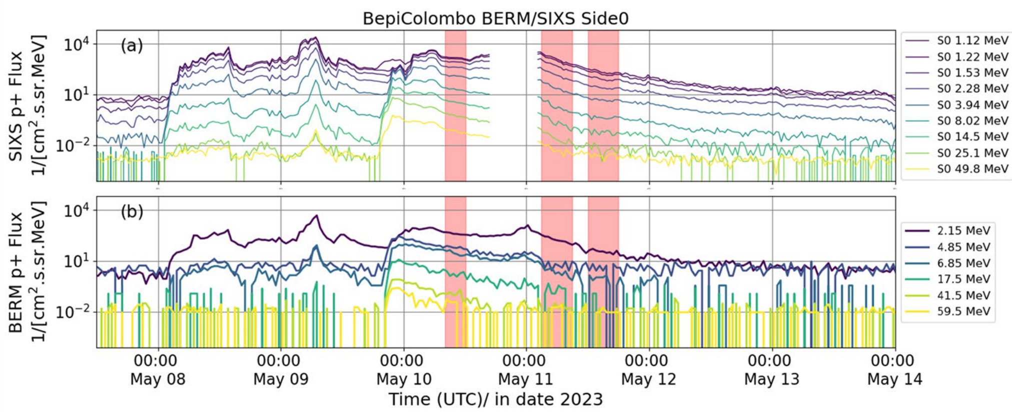

(b) 2023 May 07

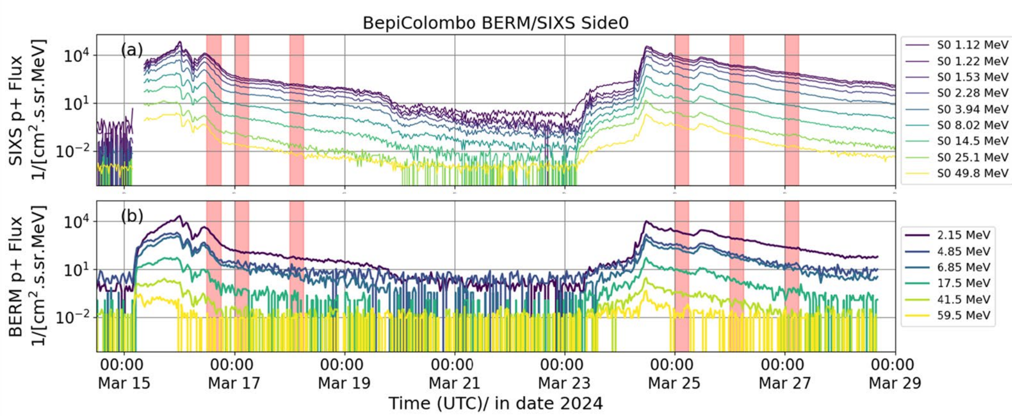

(c) 2024 March 14

Fig. 10 Combined plots for the dates presented in the subfigures

consistently high sensitivity, resulting in higher uncertainties in the calibration results.

To validate the proton calibration, BERM data were processed using the calibration parameters presented in Table 3, and the same time periods used during calibration. The resulting calibration factors for each BERM proton channel, for each event are shown in Fig. 12 as a histogram. Among the selected events, validation was

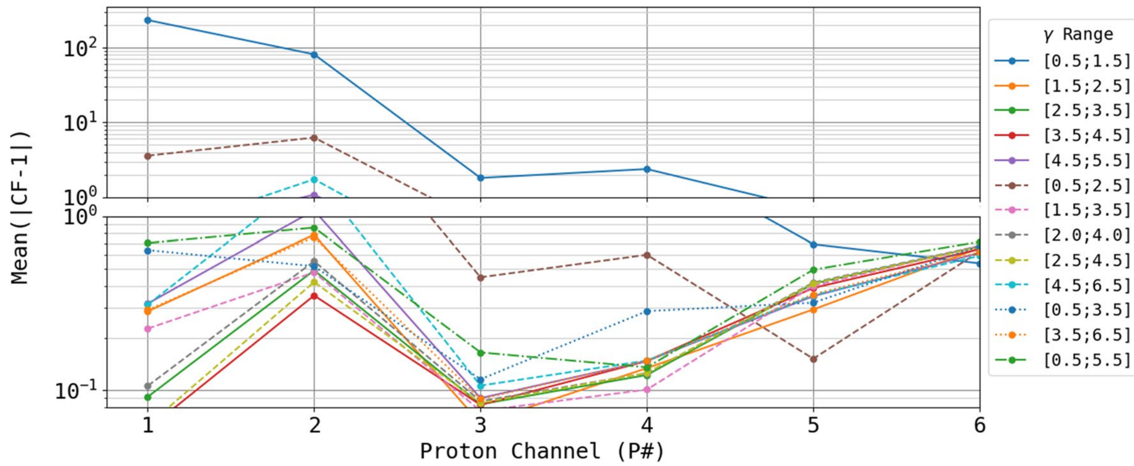

Fig. 11 Comparison of the calibration factor for different spectral index ranges used in the bow–tie method. Each line corresponds to a spectral index range and each point corresponds to the mean value of $|CF - 1|$, for all time intervals analyzed

only possible up to channel P5, since channel P6 contains data from a single event only, and channels P7 and P8 did not show particle counts above the background during the chosen time periods. Although channels P6 to P8 were calibrated using the same method as the lower channels, due to the lack of comparison possibilities with SIXS, the spectral index range used in the bow–tie method for these channels was chosen based on which range provided the best calibration agreement for channel P5.

Channels P1 to P5 exhibit mean calibration factors close to 1 (the ideal value), with varying values of dispersion. Notably, channel P2 shows a higher dispersion in calibration factors across events, which is consistent with its broad response function. As discussed by Gomes (2023) and Cardoso (2022), the response function of channel P2 remains non-negligible below 9 MeV (see Fig. 4), significantly affecting its sensitivity. This makes channel P2 more susceptible to variations in the spectral index of the incident energy spectrum compared to the other proton channels. Channels P1 and P2 also suffer from high-energy proton contamination ($E > 100$ MeV), contributing to the dispersion in the bow–tie results of these two channels. The analysis of channels P3 to P5 could benefit from more counts; however, the presented results validate the method applied in Sect. 5 for all channels up to P5. The overall dispersion is low for every channel, ensuring that the calibration factors obtained for BERM can be used for a variety of proton energy spectra.

Even though the calibration method is the same as for the proton channels, the calibration could not be validated for electron channels, due to the lack of statistical significance in the count rates detected during the events analysed.

6 Discussion

BERM is an instrument aboard ESA's BepiColombo mission that provides continuous measurements of high energy particles during all mission phases. This work presents the calibration of its electron and proton channels using the bow–tie method, enabling the conversion of count rates to particle fluxes. These results enhance BERM's capability to contribute to the scientific analysis of SEP events and the radiation environment in the inner solar system.

BERM electron channels were successfully calibrated from E1 to E3. Channels E4 and E5 could not be calibrated using the bow–tie method due to their low overall sensitivity. As anticipated from the shape of their response functions, the calibrated electron channels exhibit higher uncertainties compared to the proton channels. This is primarily because the response functions of channels E1 and E2 do not display a well-defined high sensitivity plateau, but rather a single prominent sensitivity peak around ~0.25 MeV, sufficiently high to treat the channels as differential. Channel E3 also presents elevated uncertainties, due to the smooth transition between low and high sensitivity regions in the response function. Nevertheless, the results from these three electron channels show uncertainties below 6% in the determined geometric factor, which is considered a satisfactory calibration outcome.

Proton channels were also successfully calibrated. For protons, the choice of spectral index range in the bow–tie method was optimized by comparing multiple calibration analyses with SIXS measurements, using several 6-h time windows across three SEP events. The final calibration for each proton channel was defined by selecting the index range that yielded the best correlation with

Table 3 Characteristic energies and geometric factors of BERM channels. E_{eff} and GdE or GI correspond to the point in the bow–tie distribution functions that minimize the normalized standard deviation σ, of the distribution (represented as a vertical dashed line in Fig. 7). The errors $\delta-$ G and $\delta+$ G correspond to the fifth and ninety-fifth percentile of the distribution subtracted by the mean value

Name	Type	E_{eff} (MeV)	GdE ($cm^2 \cdot sr \cdot MeV$)	G_I ($cm^2 \cdot sr$)	$\sigma_{\min}$	δ_G^-	δ_G^+	$\%\delta_G^-$	$\%\delta_G^+$
E1	Diff	0.28	$7.79 \cdot 10^{-6}$	–	0.090	$-1.91 \cdot 10^{-7}$	$3.14 \cdot 10^{-7}$	−2.45%	4.03%
E2	Diff	0.36	$4.26 \cdot 10^{-5}$	–	0.109	$-1.52 \cdot 10^{-6}$	$2.53 \cdot 10^{-6}$	−3.56%	5.93%
E3	Int	0.35	–	$8.03 \cdot 10^{-7}$	0.090	$-3.79 \cdot 10^{-8}$	$5.93 \cdot 10^{-8}$	−3.19%	4.99%
P1	Diff	2.15	$9.40 \cdot 10^{-4}$	–	0.017	$-4.36 \cdot 10^{-6}$	$1.06 \cdot 10^{-5}$	−0.46%	1.08%
P2	Diff	4.85	$3.11 \cdot 10^{-4}$	–	0.050	$-5.12 \cdot 10^{-6}$	$8.73 \cdot 10^{-6}$	−1.65%	2.81%
P3	Diff	6.85	$1.17 \cdot 10^{-3}$	–	0.007	$-2.05 \cdot 10^{-6}$	$4.85 \cdot 10^{-6}$	−0.18%	0.41%
P4	Diff	17.5	$3.00 \cdot 10^{-3}$	–	0.084	$-7.73 \cdot 10^{-5}$	$1.46 \cdot 10^{-4}$	−2.18%	4.12%
P5	Diff	41.5	$2.70 \cdot 10^{-2}$	–	0.249	$-2.16 \cdot 10^{-3}$	$3.81 \cdot 10^{-3}$	−8.01%	14.14%
P6	Diff	59.5	$4.58 \cdot 10^{-2}$	–	0.123	$-1.82 \cdot 10^{-3}$	$3.16 \cdot 10^{-3}$	−3.98%	6.91%
P7	Diff	87.5	$4.69 \cdot 10^{-2}$	–	0.060	$-9.43 \cdot 10^{-4}$	$1.62 \cdot 10^{-3}$	−2.01%	3.46%
P8	Diff	123.5	$8.49 \cdot 10^{-2}$	–	0.048	$-1.35 \cdot 10^{-3}$	$2.30 \cdot 10^{-3}$	−1.60%	2.71%

the SIXS proton fluxes. This approach resulted in low uncertainties for the geometric factors in most channels. Channel P5 shows the largest uncertainties (−8.01% and 14.14%) due to the small difference between its high and low sensitivity levels, leading to an effective energy outside its nominal high-sensitivity range ($E_{\text{eff}} = 41.5$ MeV for a range of ∼[19, 31] MeV). A similar effect is observed in channel P2, with $E_{\text{eff}} = 4.85$ MeV for a range of ∼[9, 13] MeV, although its uncertainties are lower (−1.65% and 2.81%).

Calibration validation with SIXS data was possible for proton channels up to P5 using the same SEP events used for calibration. Ideally, calibration and validation should be performed using independent SEP events; however, due to the very limited number of suitable events (only three with sufficiently high fluxes and with SIXS operating), this was not possible. Nevertheless, the low dispersion in the calibration factors, except for channel P2 (Fig. 12) across different SEP events, each characterized by distinct energy spectra, suggests that the quality of the calibration obtained in this work is robust and does not strongly depend on the specific spectral shape of the SEP event, although a dedicated analysis of individual solar events may yield small differences in the results, particularly when the spectral index differs significantly from those considered in this analysis. The comparison gives confidence to the method developed to calibrate BERM. It also gives confidence that flux reconstruction for other channels is reasonable, even though no dedicated validation has been made, since the same method is applied. As a result, channels P1 to P5 show calibration factors close to 1 (ideal case), with dispersions from 7% up to 29% in the case of channel P2. The observed dispersion can be explained in two ways: first, the limited statistics of the validation dataset, since not all time windows contained data for all channels, resulting in lower statistics for higher energy channels, and second, in the case of channel P2, which is sensitive to a wide energy range of primary particles, the bow–tie method becomes less precise, as it assigns a single effective energy and geometric factor to characterise the channel. This fact contributes to its broad range of non-negligible sensitivity.

7 Conclusions

In this work, some BERM electron channels (E1 to E3) and all proton channels were calibrated using the bow–tie method, with the results summarised in Table 3. For proton channels P1 to P5, the calibration was further validated through comparison with SIXS measurements during three SEP events, yielding calibration factors of 1.06 ± 0.14, 0.96 ± 0.29, 1.03 ± 0.15, 0.96 ± 0.07, and 0.95 ± 0.16, respectively. The close agreement between BERM and SIXS strengthens confidence in the method used in this work to calibrate BERM channels, as well as in BERM's measurements themselves, particularly for SEP event analysis. These results demonstrate that, despite being primarily designed as a housekeeping instrument, BERM can provide scientifically valuable data and make meaningful contributions to heliospheric science studies. The calibration presented in this work was performed during the cruise phase of the mission; however, no change is foreseen after the mission enters Mercury's orbit and separates the spacecraft.

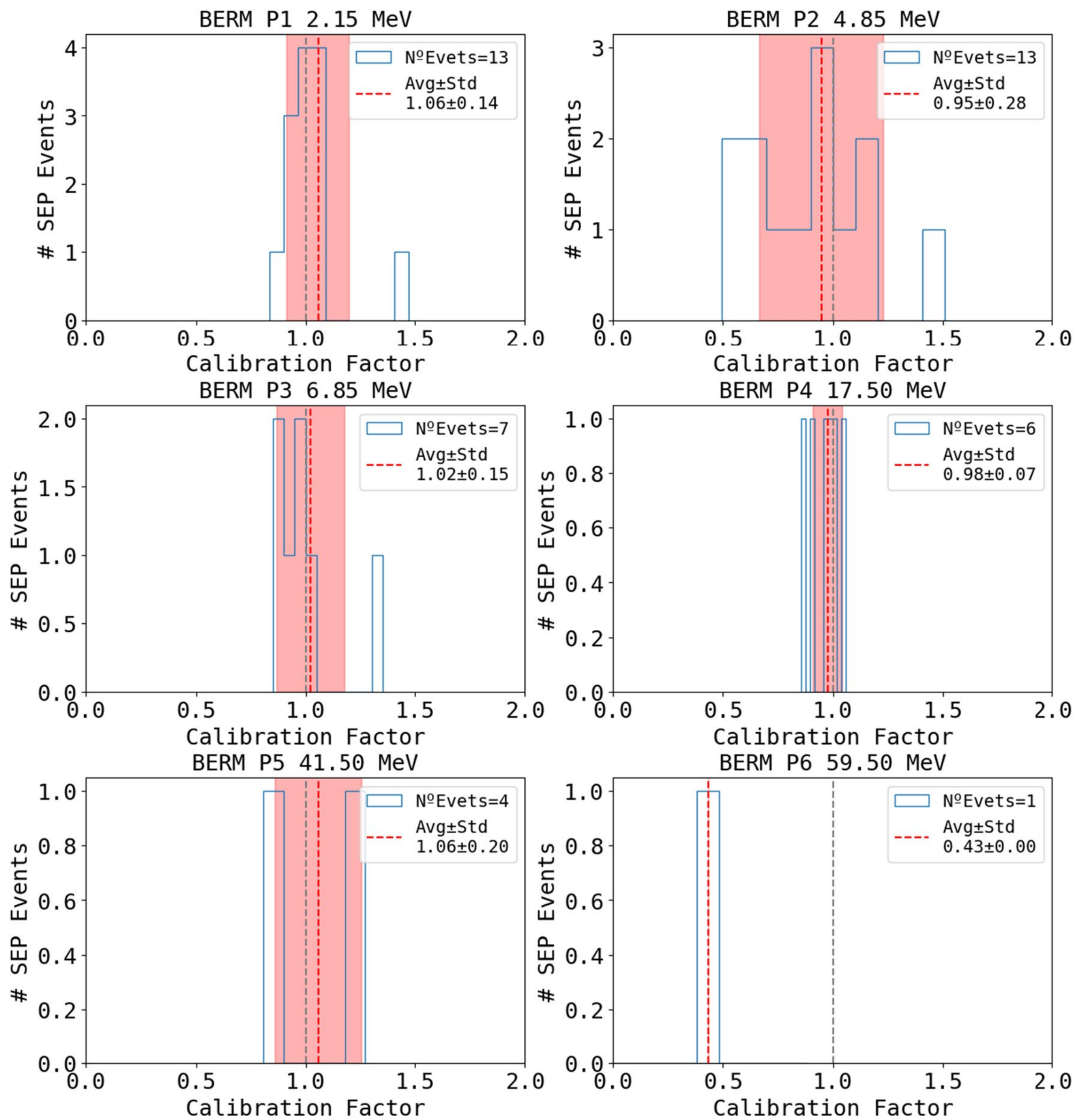

Fig. 12 Histogram showing the distribution of calibration factors for each channel, based on the time intervals analyzed. The number of intervals considered for each channel depends on whether the event was successfully detected in that specific channel. The vertical dashed gray line represents the ideal calibration factor (CF = 1), while the vertical dashed red line indicates the mean calibration factor. The red shaded area corresponds to one standard deviation from the mean

Appendix A. BERM and SIXS energy spectrums

For each time period mention in Sect. 5.2 a proton energy spectrum was computed for SIXS proton data. The spectrums are presented in Figs. 13, 14 and 15.

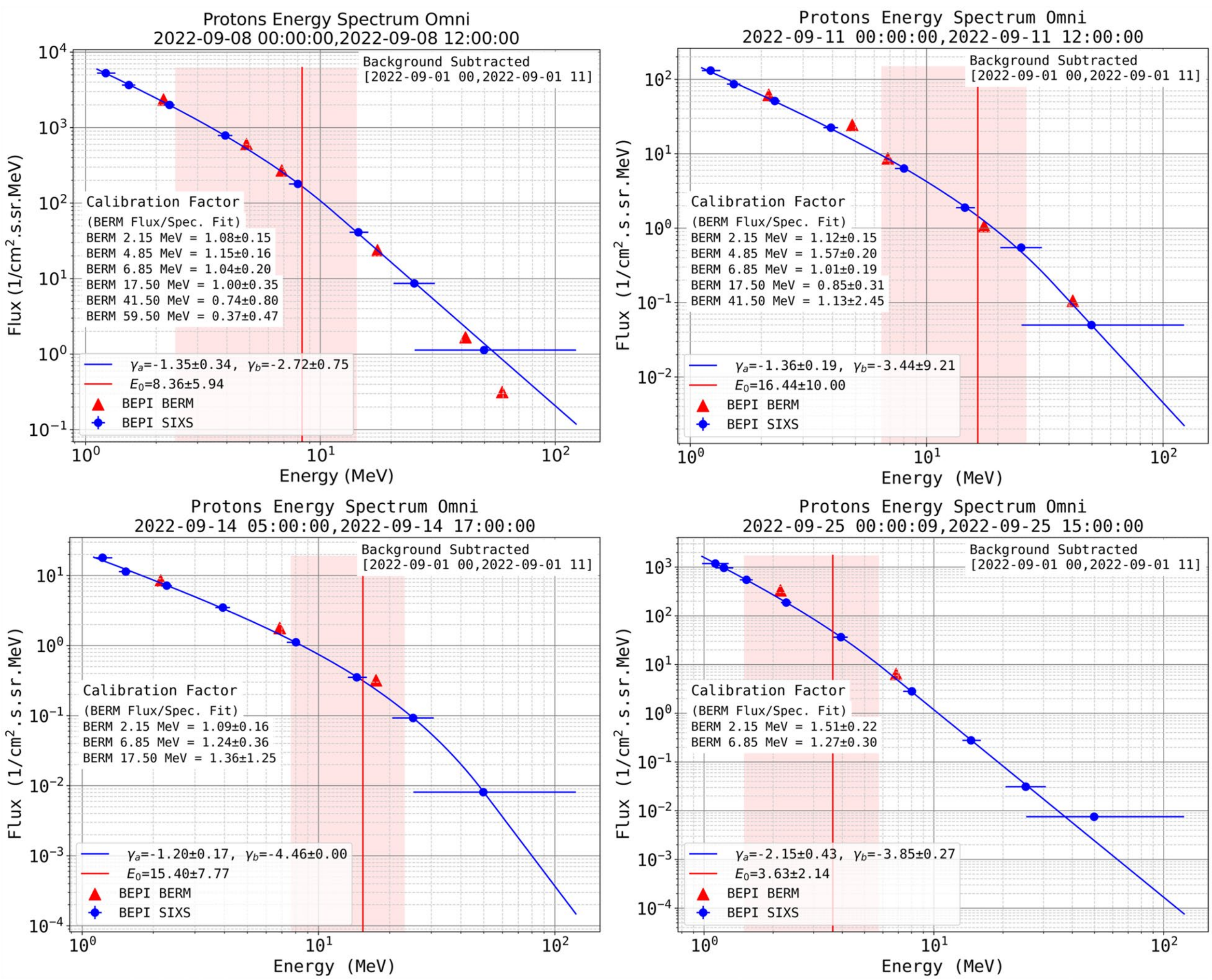

Fig. 13 BERM energy spectrum (with background subtracted) with a calibration based on best spectral index range for each channel and omnidirectional SIXS energy spectrum, with SIXS band function (Band et al. 1993; Yu et al. 2022) fit parameters. Blue horizontal lines indicate SIXS channels' energy range, red vertical line and shading indicates the energy break and its uncertainty energy range, and the calibration factor are indicated as "BERM E_{eff} MeV = CF±UNC"

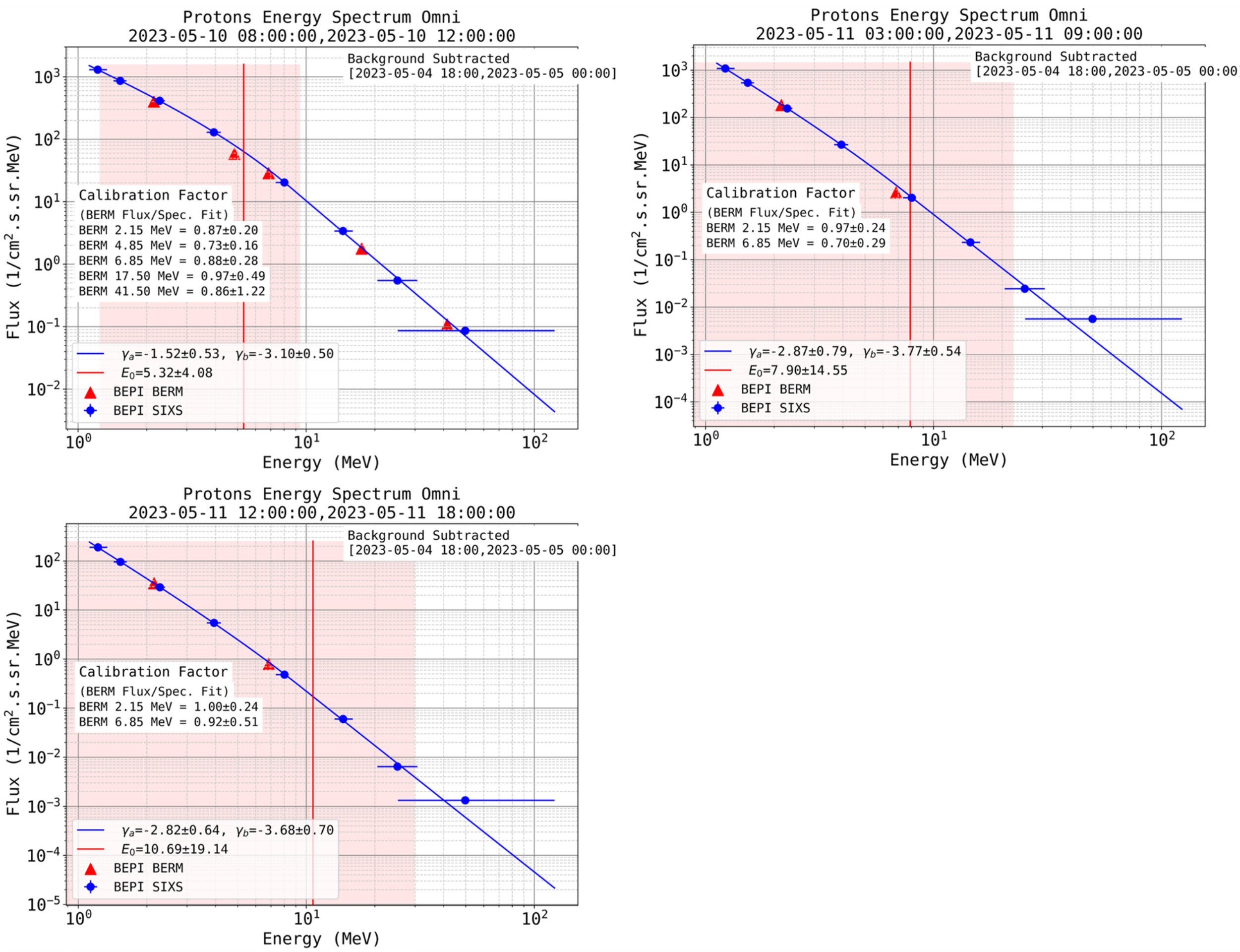

Fig. 14 BERM energy spectrum (with background subtracted) with a calibration based on best spectral index range for each channel and omnidirectional SIXS energy spectrum, with SIXS band function (Band et al. 1993; Yu et al. 2022) fit parameters. Blue horizontal lines indicate SIXS channels' energy range, red vertical line and shading indicates the energy break and its uncertainty energy range, and the calibration factor are indicated as "BERM E_{eff} MeV = CF±UNC"

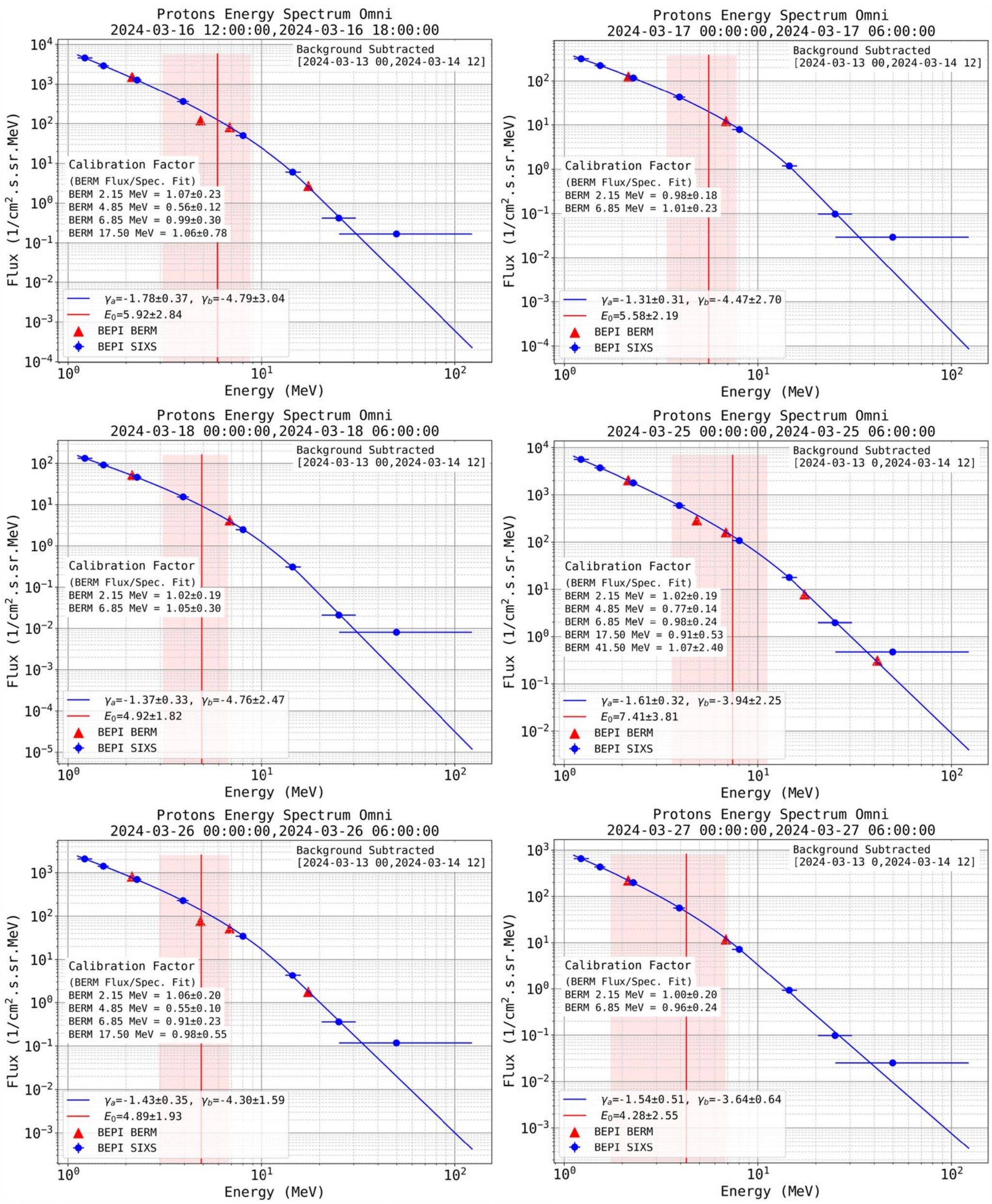

Fig. 15 BERM energy spectrum (with background subtracted) with a calibration based on best spectral index range for each channel and omnidirectional SIXS energy spectrum, with SIXS band function (Band et al. 1993; Yu et al. 2022) fit parameters. Blue horizontal lines indicate SIXS channels' energy range, red vertical line and shading indicates the energy break and its uncertainty energy range, and the calibration factor is indicated as "BERM E_{eff} MeV = CF±UNC"

Acknowledgements
This work was funded by the Portuguese Foundation for Science and Technology (FCT) through the research grant no. UI/BD/154,742/2023, under the framework of the project 'Advanced Methods for Solar Energetic Particle Events Characterization in the Inner Solar System' and ESA: 4,000,137,865/22/ES/JDExpert Suport to BERM & RADEM units. This work was carried out by the joint research program of the Institute for Space-Earth Environmental Research, Nagoya University. This work was performed using the facilities of Institute for Space-Earth Environmental Research, Nagoya University. B.S.-C. acknowledges support through STFC Ernest Rutherford Fellowship ST/V004115/1 and STFC grant ST/Y000439/1. N.D. is grateful for support from the Research Council of Finland (SHOCKSEE, grant No. 346,902 and AIPAD, grant No. 368,509). The study reflects only the authors' view and the European Commission is not responsible for any use that may be made of the information it contains.

Author Contributions
A.G. wrote the first draft of this paper and performed all the numerical analysis. M.P. contributed to the study design, data analysis, writing, and reviewed on this paper. C.C. and P.G. contributed to the data analysis. R.V., J.G. and N.D. contributed with SIXS data support and reviewed on this paper. B.S-C and A.M.

reviewed on this paper. E.E., E.K, A.L., P.O and C.P contributed for the SIXS data collection.

Funding
Work in the University of Turku and University of Helsinki was performed under the umbrella of Finnish Centre of Excellence in Research of Sustainable Space (FORESAIL) funded by the Research Council of Finland (grants No. 352,847, 352,850).
We acknowledge funding by the European Union's Horizon 2020/Horizon Europe research and innovation program under grant agreement No. 101,004,159 (SERPENTINE) and No. 101,134,999 (SOLER) and No. 101,135,044 (SPEARHEAD).

Data Availability
The datasets generated and/or analysed during the current study are not currently publicly available due to processing of the archiving, but are available from the corresponding author on reasonable request.

Declarations

Competing interests
The author declares no competing interests.

Author details
[1]Laboratory for Instrumentation and Experimental Particle Physics (LIP), Lisboa, Portugal. [2]Instituto Superior Técnico, University of Lisbon, Lisbon, Portugal. [3]Department of Physics and Astronomy, University of Turku, Turku, Finland. [4]Department of Physics, University of Helsinki, Helsinki, Finland. [5]School of Physics and Astronomy, University of Leicester, Leicester, UK. [6]University of Aveiro, Aveiro, Portugal.

Received: 6 October 2025 Accepted: 2 April 2026
Published online: 02 June 2026

References
Agostinelli S, Allison J, Amako K et al (2003) Nuclear Instruments and Methods in Physics Research Section A: Accelerators, Spectrometers. Detec Ass Equip 506:250
Anderson BJ, Johnson CL, Korth H et al (2011) Science 333:1859
Arruda L, Gonçalves P, Sandberg I, et al (2016) in 2016 16th European Conference on Radiation and Its Effects on Components and Systems (RADECS), 1–4
Band D, Matteson J, Ford L et al (1993) ApJ 413:281
Barth J, Dyer C, Stassinopoulos E (2003) Nuclear Science. IEEE Trans 50:466
Baumjohann W, Matsuoka A, Magnes W, et al (2010) Planetary and Space Science, 58, 279, comprehensive Science Investigations of Mercury: The scientific goals of the joint ESA/JAXA mission BepiColombo
Baumjohann W, Matsuoka A, Narita Y et al (2020) Space Sci Rev 216:125
Benkhoff J, Murakami G, Baumjohann W et al (2021) Space Sci Rev 217:90
Boudouridis A, Rodriguez J, Kress B, Dichter B, Onsager T (2020) Space Weather, 18, e2019SW002403, e2019SW002403 2019SW002403
Bunce EJ, Martindale A, Lindsay S et al (2020) Space Sci Rev 216:126
Cardoso C (2022) PhD thesis, Instituto Superior Técnico
Chitta LP, Zhukov AN, Berghmans D et al (2023) Science 381:867
Clette F, Lefèvre L, (2015) SILSO Sunspot Number V2.0, https://doi.org/10.24414/qnza-ac80, published by WDC SILSO - Royal Observatory of Belgium (ROB)
Dodd P, Massengill L (2003) IEEE Trans Nucl Sci 50:583
Dresing N, Effenberger F, Gómez-Herrero R et al (2020) Astrophys J 889:143
Emslie AG, Kucharek H, Dennis BR, et al (2004) Journal of Geophysical Research: Space Physics, 109
Fraser G, Carpenter J, Rothery D, et al (2010) Planetary and Space Science, 58, 79, comprehensive Science Investigations of Mercury: The scientific goals of the joint ESA/JAXA mission BepiColombo
Gomes A (2023) PhD thesis, Instituto Superior Técnico
Heyner D, Auster H-U, Fornaçon K-H et al (2021) Space Sci Rev 217:52
Hiesinger H, Helbert J (2010) Planetary and Space Science, 58, 144, comprehensive Science Investigations of Mercury: The scientific goals of the joint ESA/JAXA mission BepiColombo
Ho GC, Krimigis SM, Gold RE et al (2011) Science 333:1865
Honig T, Witasse OG, Evans H et al (2019) Ann Geophys 37:903
Huovelin J, Vainio R, Kilpua E et al (2020) Space Sci Rev 216:94
Iafolla V, Fiorenza E, Lefevre C, et al (2010) Planetary and Space Science, 58, 300, comprehensive Science Investigations of Mercury: The scientific goals of the joint ESA/JAXA mission BepiColombo
Jun I, Garrett HB, Evans RW (2019) IEEE Trans Plasma Sci 47:3923
Kahler SW (2007) Space Sci Rev 129:359
Kasaba Y, Bougeret J-L, Blomberg L, et al (2010) Planetary and Space Science, 58, 238, comprehensive Science Investigations of Mercury: The scientific goals of the joint ESA/JAXA mission BepiColombo
Kasaba Y, Kojima H, Moncuquet M et al (2020) Space Sci Rev 216:65
Khoo LY, Sánchez-Cano B, Lee CO et al (2024) ApJ 963:107
Kobayashi M, Shibata H, Nogami K et al (2020) Space Sci Rev 216:144
Lawrence DJ, Anderson BJ, Baker DN et al (2015) J Geophys Res Space Physics 120:2851
Lucente M, Lefevre C, Fiorenza E et al (2022) Planet Space Sci 211:105396
McNutt RL, Solomon SC, Gold RE, Leary JC (2006) Advances in Space Research, 38, 564, mercury, Mars and Saturn
Milillo A, Fujimoto M, Murakami G, et al (2020) Space Science Reviews, 216
Mohammadzadeh A, Evans H, Nieminen P et al (2003) IEEE Trans Nucl Sci 50:2272
Murakami G, Hayakawa H, Ogawa H et al (2020) Space Sci Rev 216:113
Nogami K, Fujii M, Ohashi H, et al (2010) Planetary and Space Science, 58, 108, comprehensive Science Investigations of Mercury: The scientific goals of the joint ESA/JAXA mission BepiColombo
Oldham T, McLean F (2003) IEEE Trans Nucl Sci 50:483
Oleynik P (2021) PhD thesis, University of Turku
Oleynik P, Palmroos C, Gieseler J, Vainio R (2024) A description of the BepiColombo/SIXS-P cruise phase data product
Orsini S, Livi S, Torkar K, et al (2010) Planetary and Space Science, 58, 166, comprehensive Science Investigations of Mercury: The scientific goals of the joint ESA/JAXA mission BepiColombo
Pinto M, Poivey C, Donadoni M, et al (2025) IEEE Transactions on Nuclear Science, 1
Pinto M, Sanchez-Cano B, Moissl R, et al (2022) Space Science Reviews, 218
Potgieter MS (2013) Living Rev Sol Phys 10:3
Raukunen O, Paassilta M, Vainio R et al (2020) Journal of Space Weather and Space Climate 10:24
Reames DV (1999) Space Sci Rev 90:413
Reames DV, Kahler SW, Ng CK (1997) Astrophys J 491:414
Rodríguez-García L, Gómez-Herrero R, Dresing N et al (2025) A&A 694:A64
Saito Y, Sauvaud J, Hirahara M, et al (2010) Planetary and Space Science, 58, 182, comprehensive Science Investigations of Mercury: The scientific goals of the joint ESA/JAXA mission BepiColombo
Selesnick RS, Blake JB (2000) J Geophys Res Space Physics 105:2607
Srour J, Marshall C, Marshall P (2003) IEEE Trans Nucl Sci 50:653
Strauss RD, Dresing N, Kollhoff A, Brüdern M (2020) ApJ 897:24
Sánchez-Cano B, Hadid LZ, Aizawa S et al (2025) Earth. Planets and Space 77:114
Thomas N, Hussmann H, Spohn T et al (2021) Space Sci Rev 217:25
Van Allen JA, Baker DN, Randall BA, Sentman DD (1974) J Geophys Res 79:3559
Yardley SL, Brooks DH, D'Amicis R et al (2024) Nature Astronomy 8:953
Yu F, Kong X, Guo F et al (2022) The Astrophy J Let 925:L13

Publisher's Note